Supporting information

Large-area Graphene Realizing Ultrasensitive Photothermal Actuator with High Transparency: New Prototype Robotic Motions Under Infrared-Light Stimuli **

Table of contents

S1. The fabrication of Infrared-motivated artificial worm

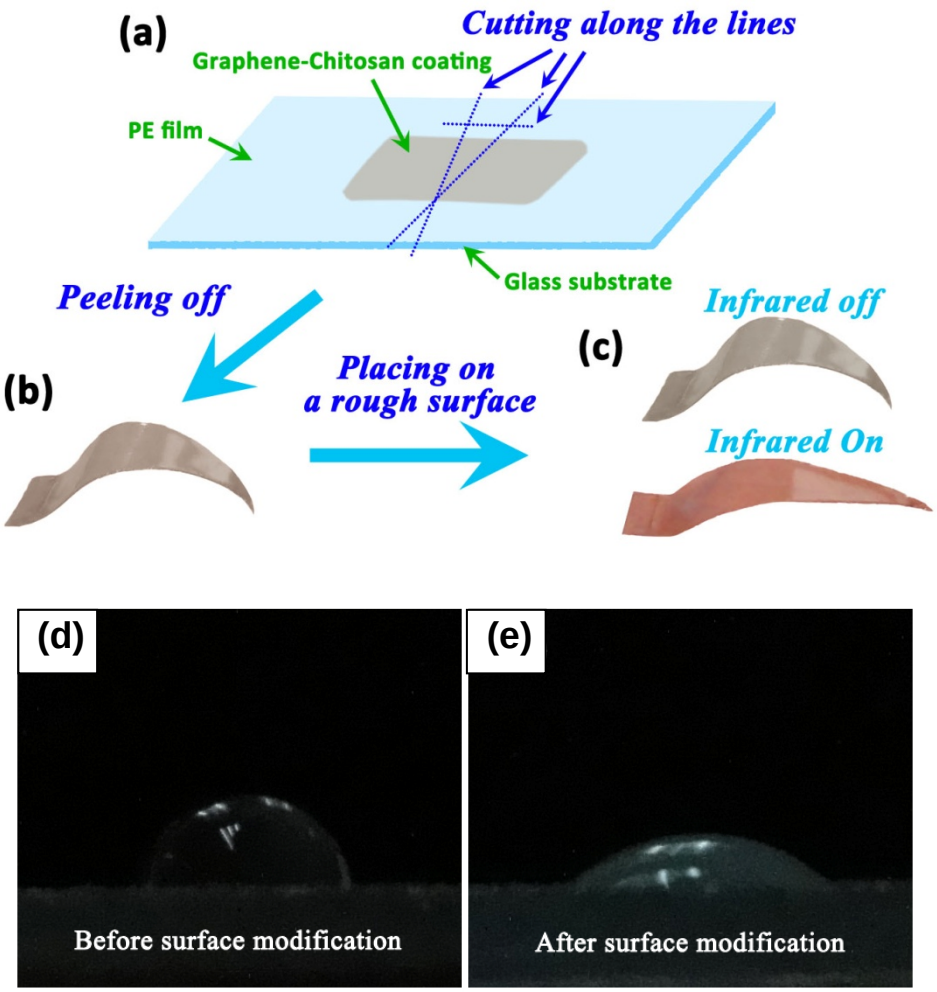

Figure S1. A schematic procedure for the fabrication of the infrared-triggered artificial worms. (a) A triangle-shaped area was cut out as is shown by the dashed lines. (b) The cut-out area was peeled off, after which the strip automatically transformed in to a bended state. (c) The two different states with and without infrared radiation, which shows a typical crawling mechanism like the real worms. (d-e) Comparison of the contact angle for PE thin film before (d) and after (e) surface modification by the oxidative mixture of H_2SO_4, HNO_3 and CrO_3.

S2. Characterization of the graphite oxide (GO) and graphene sample

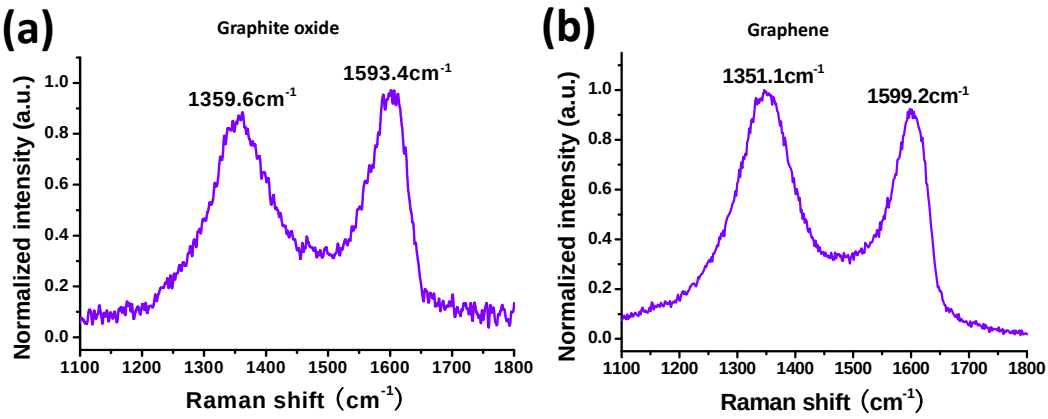

Figure S2. (a) Raman spectrum of the as-synthesized graphite oxide (GO), recorded using 514 nm laser excitation. The two characteristic peaks at ~1593.4cm^{-1} and ~1359.6cm^{-1} can be attributed to the G band and D band of graphite oxide, respectively, which were in good consistence with the literature.[1] (b) Raman spectrum of the as-prepared graphene, recorded using 514nm laser excitation. The D band and G band peaks of graphene shift to 1351.1cm^{-1} and 1599.2cm^{-1}, respectively, with an increased D/G intensity ratio compared to that of GO, as was reported in previous literatures.[2]

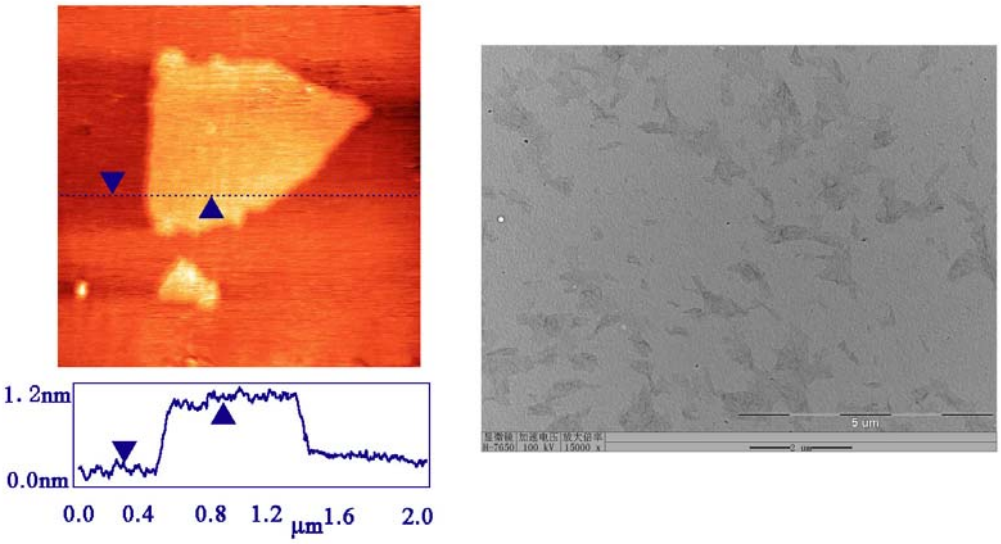

Figure S3. Characterization of nanosized graphene sample by AFM and TEM images. (a) Tapping mode atomic force microscope (AFM) image and height profile of the graphene sample; vertical distance between the two blue triangle marks is ~ 0.98 nm, clearly showing an intrinsic single-layered structure. (b) TEM image of the as-synthesized nanosized graphene with well dispersion.

S3. Optical and mechanical characterization of the large-area graphene-chitosan/PE thin film

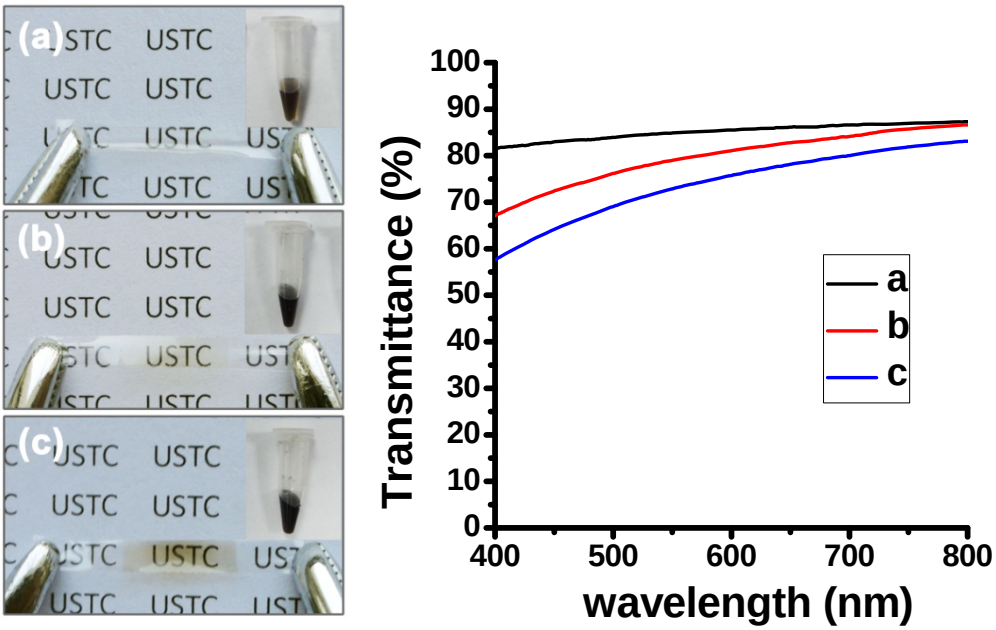

Figure S4. Large-area Graphene-Chitosan/PE thin films with increasing large-area graphene content. Graphene contents incorporated in the actuator strips are (a) 5.21 μg/mm^3, (b) 10.42 μg/mm^3 and (c) 15.63 μg/mm^3, as percentages of weight, and the inset photographs show the corresponding starting graphene/chitosan mixture. This comparison experiment clearly demonstrates that our bimorph actuator strip could keep a considerable high transparency even with a graphene concentration as high as 15.63 μg/mm^3. In our work, the film shown in (a) was used to conduct all the characterization measurements, clearly showing that the transparent thin film with very low large-area graphene concentration could well display high IR absorbing ability. These results indicated that graphene is not only a fabulous material to fabricate transparent devices, but also a good IR-capturing material.

S4. Mechanical property of large-area graphene based bimorph configuration

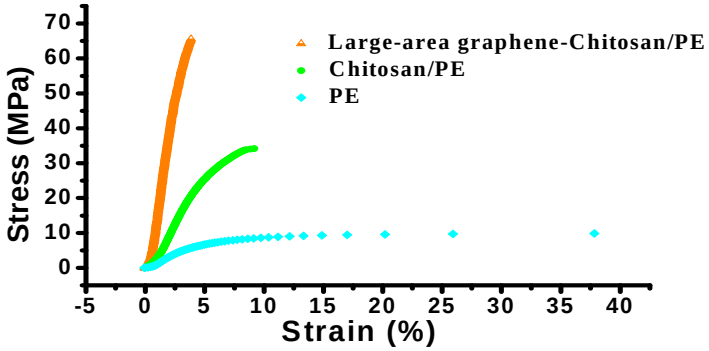

Figure S5. Representative stress-strain behavior of graphene-chitosan/PE, chitosan/PE and pure PE film, respectively.

The incorporated large-area graphene largely reinforces the bimorph strip with improved mechanical properties, which guarantees the high stability performance of our as-established transparent actuators. The mechanical behaviors of the actuator strip (graphene-chitosan/PE), chitosan/PE film and pure PE film were investigated by tensile tests at room temperature, and the typical stress-strain curves are shown in **Figure S5**. The graphene-involving significantly improved the tensile properties of the actuator strip, even toward a maximum tensile stress of 66 MPa, which is almost twice as much as that of chitosan/PE film (34 MPa), and seven times larger than that of pure PE film (9.8 MPa). Of note, the very few graphene contents in our transparent actuator (only 5.21 $\mu g/mm^3$ graphene in the whole strip) significantly improved the mechanic properties in our actuator strip.

S5. Infrared-light power density dependent of degree of deformation

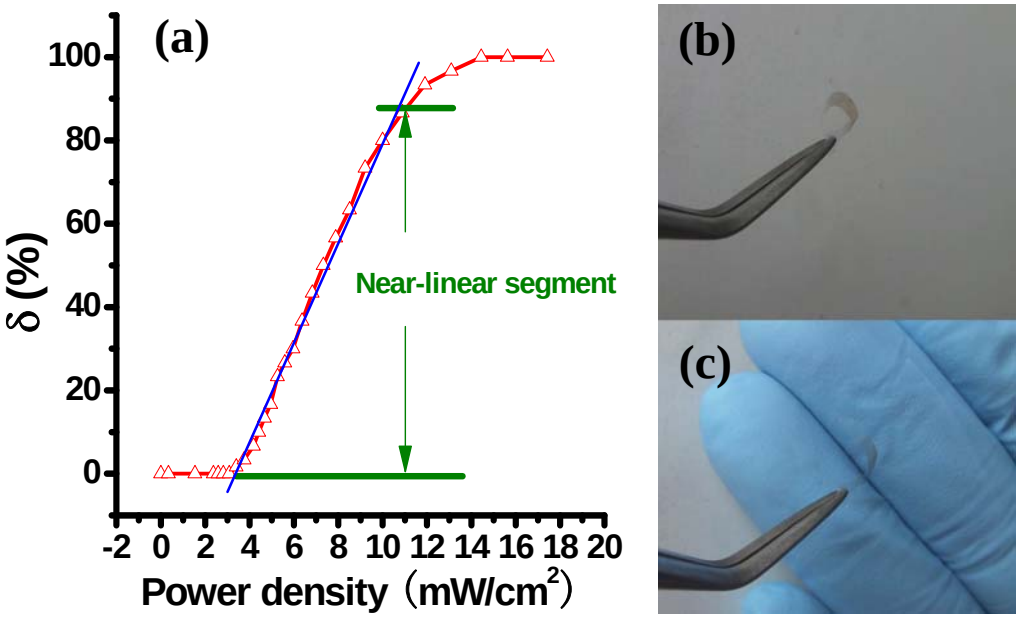

Figure S6. (a) Infrared-light power density dependent of degree of deformation (%) at the given bearing force of 0.2 mN. The energy power density delivered to the bimorph thin film was measured by a light intensity meter. As is shown, when the power density of applied IR was changed from 3 mW/cm^2 to 16 mW / cm^2, the degree of deformation δ (%) increased from ~5 % to 100 %, showing a perfect linear correlation between δ (%) and the applied infrared power density in a wide power density range from 4 mW/cm^2 to 16 mW / cm^2. (b-c) Even under the very weak IR irradiation by the hand approaching, the actuator exhibits the contracting-to-stretching behavior with high sensitivity. See the detailed experimental process in the video as an electronic supporting information.

S6. Characterization of the actuator performance

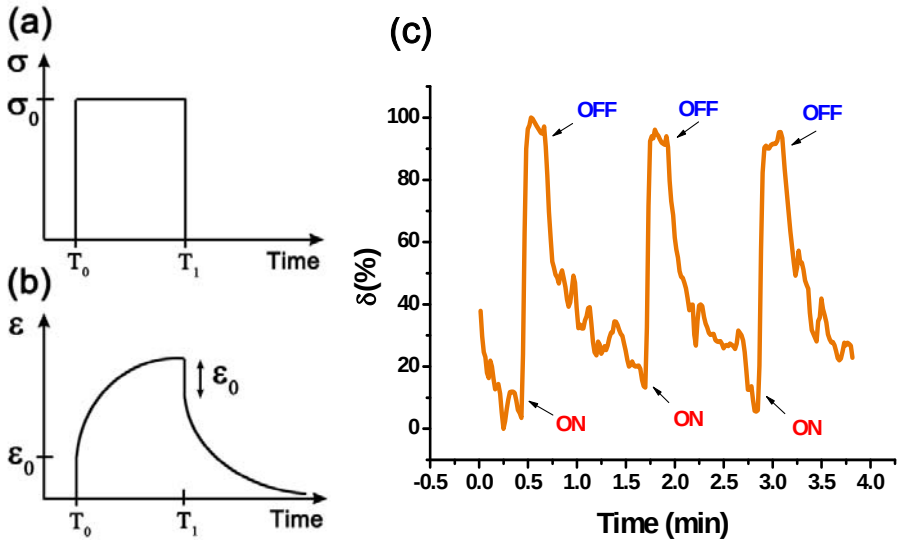

Figure S7. (a) Applied stress and (b) induced strain as functions of time over a short period for a viscoelastic material. (c) Periodic displacement changes of the actuator strip via ON-OFF switching of infrared radiation by dynamic mechanical analysis (DMA) test.

By the dynamic mechanical analysis (DMA) test as shown in **Figure S7**, the bimorph actuator that were constructed by the two layers of PE and chitosan shows the typical viscoelastic behavior.

For a typical viscoelastic material (VM), under the external response of stress, VM usually undergoes two sequent processes including the initially typical elasticity behavior (Hooke spring mechanism) and the modified elasticity behavior (Newtonian dashpot mechanism), known as Kelvin-Voigt mode.[3] In these processes, the Hooke spring elasticity usually appeared at the very short time and under the stress critical point; while the Newtonian dashpot mechanism answers for the following behavior when the stimuli time is longer enough and the stress value is above the critical point. Such two processes of a typical viscoelastic material (VM) can be described with a formula as shown in following:

$$\varepsilon(t) = \sigma C_0 + \sigma C \int_0^\infty f(\tau)[1 - \exp(-t/\tau)]d\tau$$

Where, ε=creep strain; σ= applied stress, C_0 = instantaneous creep compliance, C = creep compliance coefficient, τ= retardation time, f(τ) = distribution of retardation times.

According to the formula, within the very short time dτ that received/remove the applied stress stimuli, the $\lim_{\tau \to 0}[1 - \exp(-t/\tau)] = 0$, and thus the $\varepsilon(t) = \sigma C_0$ (Hooke spring rule); in this case, the ε(t) is linear proportional to the applied stress. When the time is long enough, the second section ($\int_0^\infty f(\tau)[1 - \exp(-t/\tau)]d\tau$) could not be neglected, thus the ε(t) is non-linear

proportional to the applied stress, involving the Newtonian dashpot mechanism in such range. The whole process could be schematically shown in **Figure 3c**, in which the induced strain (b) as a response to the applied stress (a) as functions of time over a short period for a viscoelastic material were clearly shown. In the initial applied stress, the linear curve appears; when the applied stress increases, the creep curve rate grows disproportionately faster, exhibiting a disproportionately curve until t=t1. In the same way, when the stress-removing process occurs, the viscoelastic material exhibits a linear line initially and then the disproportional curve. Such stress-removing process is similar to that stress-applying process, and both were determined by the above mentioned formula.

For our as-obtained transparent actuator with the bimorph structure of PE and chitosan, the high infrared absorption efficiency and the fast light-to-thermal energy transferring enable the whole bimorph configuration system to be immediately warmed up. In this case, the thermal expansion coefficient differences for the bimorph configuration produced an abrupt force in a very short time. In fact, in the infrared light ON process, it approached $\tau \rightarrow 0$, and thus it was Hooke spring elasticity exhibiting linear line as indicated by red arrow in **Figure S7c**. In the infrared OFF condition, the relative slower temperature decreasing rate occurred; the two processes were clearly shown. In such process, the initial linear line and then the disproportional curve indicates the Hookean spring behavior occurs at first and then the disproportional Newtonian dashpot behavior occurs, respectively.

In effect, when the external stimuli frequency is high enough, that is, the stress applied/removed time is short enough, the symmetric linear behavior would occur in both sides of infrared light on/off states. That is to say, the bimorph-configuration actuator is the Hooke spring elasticity during the whole shape change process. As expected, at the infrared switching frequency of 1Hz, the perfect symmetric linear curves were clearly shown in **Figure S7c**, and indeed such symmetric behavior shows expected stability.

S7. Basic concepts and formula expressions for a typical bimorph model

Consider a bimorph model with two layers of layer 1 and layer 2, we choose the flat bilayer configuration under IR irradiation as a reference state. After removal of the IR irradiation, the mismatch strain ε_T can be induced by a temperature change from initial temperature T_0 to T if their linear thermal expansion coefficients $\alpha 1$ and $\alpha 2$ are different:

$$\varepsilon_T = (\alpha_1 - \alpha_2)(T - T_0). \tag{S-1}$$

By using thin film mechanics [4], in the Kirchhoff approximation the total strain energy of the bilayer induced by the thermal mismatch can be written as a function of the mid-plane strain (ε_0) and the curvature (k):

$$\frac{U}{LW} = \left\{ M_1 \left(\varepsilon_0^2 h_1 + \frac{k^2}{12} h_1^3 \right) + M_2 \left[(\varepsilon_0 + \varepsilon_T)^2 h_2 - k(\varepsilon_0 + \varepsilon_T)\left(h_2^2 + h_1 h_2\right) + \frac{k^2}{6}\left(2h_1^2 h_2 + 3h_1 h_2^2 + 2h_1^3\right) \right] \right\} \tag{S-2}$$

Where L and W are the length and width of the bilayer respectively, M_1, h_1 and M_2, h_2 are the corresponding biaxial modulus and thickness of each layer. The equilibrium shape of the bilayer is determined by the strain energy minimization through $\partial U/\partial k=0$ and $\partial U/\partial \varepsilon_0=0$:

$$k = I\left(\frac{h_2}{h_1}, \frac{M_2}{M_1}\right)\left(1 + \frac{h_2}{h_1}\right)\frac{6}{h_1}\varepsilon_T \tag{S-3}$$

$$\varepsilon_0 = -I\left(\frac{h_2}{h_1}, \frac{M_2}{M_1}\right)\left(1 + \frac{h_2^3}{h_1^3}\frac{M_2}{M_1}\right)\varepsilon_T \tag{S-4}$$

with

$$I\left(\frac{h_2}{h_1}, \frac{M_2}{M_1}\right) = \frac{h_2 M_2}{h_1 M_1}\left[1 + 4\frac{h_2}{h_1}\frac{M_2}{M_1} + 6\frac{h_2^2}{h_1^2}\frac{M_2}{M_1} + 4\frac{h_2^3}{h_1^3}\frac{M_2}{M_1} + \frac{h_2^4}{h_1^4}\frac{M_2^2}{M_1^2}\right]^{-1} \tag{S-5}$$

S8. Mechanism analysis of the independent-freestanding walking worm motivated by infrared light

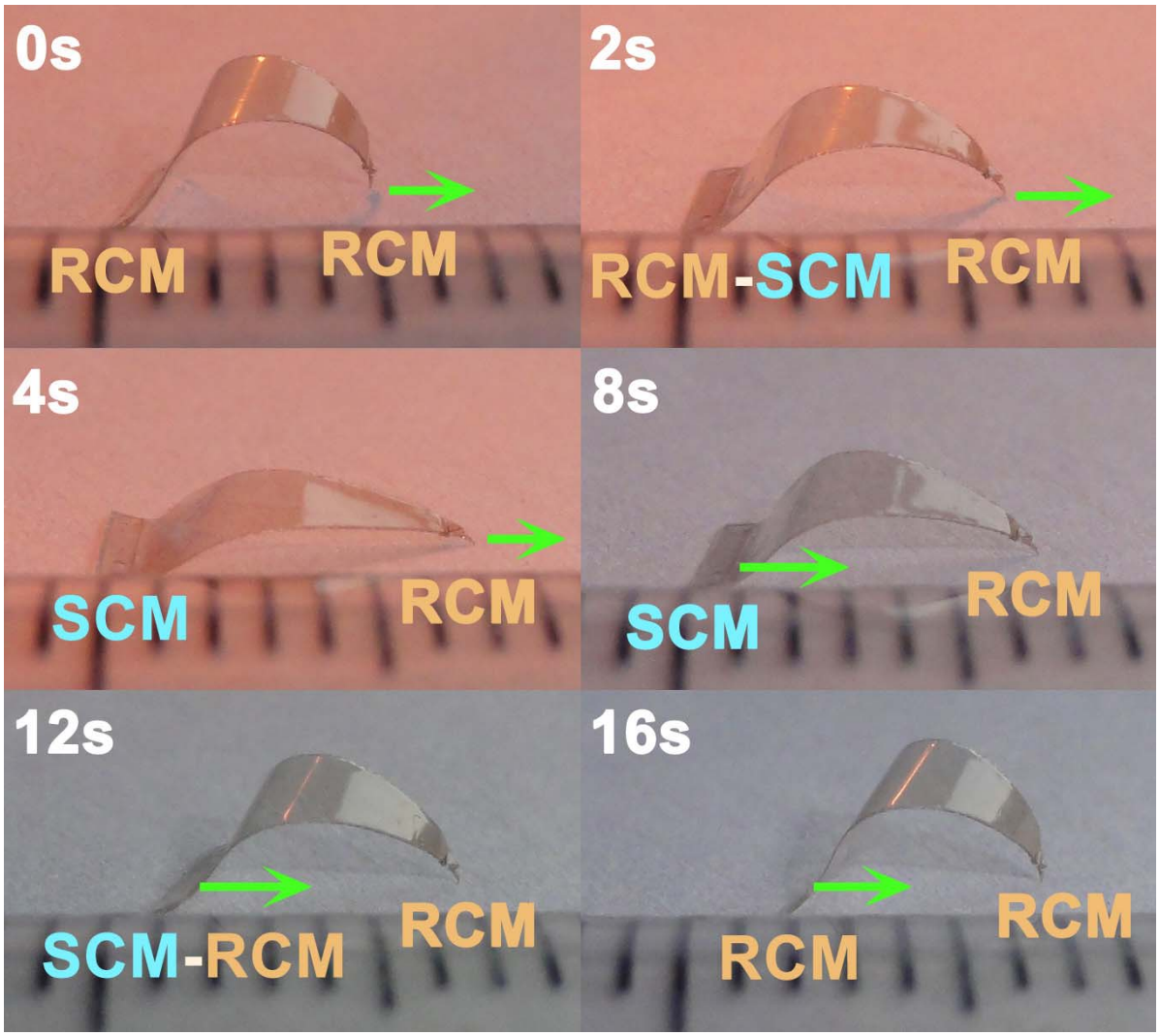

Figure S8. The magnified digital camera photograph for the time course of the typical completely-independent walking worm in a typical stretching-contracting process, clearly showing the alternating contact mode types of the rear and head edges, in which RCM and SCM are the abbreviations to Rough Contact Mode and Smooth Contact Mode, respectively.

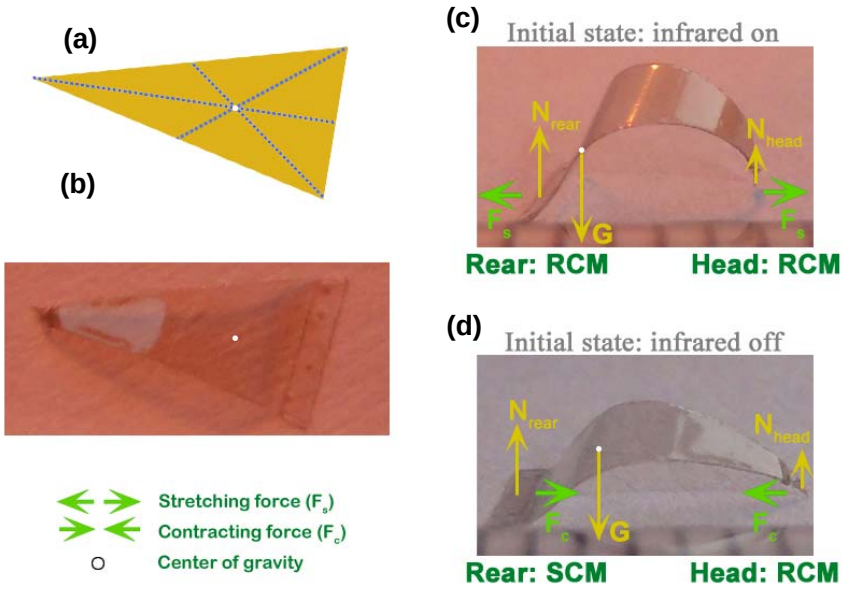

Figure S9. The force analysis of the walking worm during the stretching process under the irradiation of infrared light. (a-b) schematic illustration of the center of gravity for the as-obtained completely-independent walking worm. As can be seen, in our case, the center of gravity of the walking worm is indeed located at the position approaching to the rear side, producing the force asymmetry. (c-d) The corresponding force analysis of the initially stretching (c) / contracting (d) states.

References in the Supplementary Information

1. A. Sinitskii, A. Dimiev, D. A. Corley, A. A. Fursina, D. V. Kosynkin and J. M. Tour, *ACS Nano*, 2010, **4**, 1949-1954.
2. S. Stankovich, D. A. Dikin, R. D. Piner, K. A. Kohlhaas, A. Kleinhammes, Y. Jia, Y. Wu, S. T. Nguyen and R. S. Ruoff, *Carbon*, 2007, **45**, 1558-1565.
3. M. A. Meyers and K. K. Chawla, *Mechanical Behavior of Materials*, Cambridge University Press, 1999.
4. L. B. Freund; and S. Suresh, *Thin Film Materials: Stress, Defect Formation and Surface Evolution* Cambridge University Press, 2004.